*J. Fluid Mech.* (1983), *vol.* 131, *pp.* 319–339
*Printed in Great Britain*



# The structure of a separating turbulent boundary layer. Part 5. Frequency effects on periodic unsteady free-stream flows

By ROGER L. SIMPSON AND B. G. SHIVAPRASAD†
Department of Civil and Mechanical Engineering, Southern Methodist University, Dallas, Texas 75275

(Received 15 October 1982)

Measurements of a steady free-stream, nominally two-dimensional, separating turbulent boundary layer have been reported in earlier parts of this work. Here measurements are reported that show the effects of frequency on sinusoidal unsteadiness of the free-stream velocity on this separating turbulent boundary layer at reduced frequencies of 0.61 and 0.90. The ratio of oscillation amplitude to mean velocity is about $\frac{1}{3}$ for each flow.

Upstream of flow detachment, hot-wire anemometer measurements were obtained. A surface hot-wire anemometer was used to measure the phase-averaged skin friction. Measurements in the detached-flow zone of phase-averaged velocities and turbulence quantities were obtained with a directionally sensitive laser anemometer. The fraction of time that the flow moves downstream was measured by the LDV and by a thermal flow-direction probe.

Upstream of any flow reversal or backflow, each flow behaves in a quasisteady manner, i.e. the phase-averaged flow is described by the steady free-stream flow structure. The semilogarithmic law-of-the-wall velocity profiles applies at each phase of the cycle. The Perry & Schofield (1973) velocity-profile correlations fit the mean and ensemble-averaged velocity profiles near detachment.

After the beginning of detachment, large amplitude and phase variations develop through each flow. Unsteady effects produce hysteresis in relationships between flow parameters. As the free-stream velocity during a cycle begins to increase, the detached shear layer decreases in thickness, and the fraction of time $\hat{\gamma}_{pu}$ that the flow moves downstream increases as backflow fluid is washed downstream. As the free-stream velocity nears the maximum value in a cycle, the increasingly adverse pressure gradient causes progressively greater near-wall backflow at downstream locations while $\hat{\gamma}_{pu}$ remains high at the upstream part of the detached flow. After the free-stream velocity begins to decelerate, the detached shear layer grows in thickness, and the location where flow reversal begins moves upstream. This cycle is repeated as the free-stream velocity again increases.

In both unsteady flows, the ensemble-averaged detached-flow velocity profiles agree with steady free-stream profiles for the same $\hat{\gamma}_{pu\,\min}$ value near the wall when $\partial\hat{\gamma}_{pu\,\min}/\partial\hat{t} < 0$. However, the reduced-frequency $k = 0.90$ flow has much larger hysteresis in ensemble-averaged velocity profile shapes when $\partial\hat{\gamma}_{pu\,\min}/\partial t \geqslant 0$. Larger and negative values of the profile shape factor $\hat{H}$ occur for this flow during phases when the non-dimensional backflow is greater and $\hat{\gamma}_{pu\,\min} \rightarrow 0.01$.

† Present address: Elliott Co., Jeannette, PA 15644, U.S.A.

## 1. Introduction

The paper is the fifth part of a series that documents the behaviour of turbulent boundary layers on flat surfaces that separate due to adverse pressure gradients. Simpson, Chew & Shivaprasad (1981*a*, *b*) in parts 1 and 2, and Shiloh, Shivaprasad & Simpson (1981) in part 3 reported extensive measurements of a steady free-stream separating turbulent boundary layer produced on the floor of the wind-tunnel test section. The Reynolds number for that flow was $4.7 \times 10^6$, based on the entrance free-stream velocity $\overline{U}_{ei}$ of 15.06 m/s and the 4.9 m length $C$ of the converging–diverging section. Simpson, Shivaprasad & Chew (1983) in part 4 reported the effects of sinusoidal unsteadiness of the free-stream velocity on this separating turbulent boundary layer at a reduced frequency $k = \omega C/2\overline{U}_{ei}$ of 0.61. The ratio of oscillation amplitude to mean velocity was about 0.3.

In this current part, some effects of reduced frequency on the flow structure are examined. Measurements are reported for the same oscillation frequency (0.596 Hz), but with a mean entrance free-stream velocity $\overline{U}_{ei}$ of 10.18 m/s. The ratio of oscillation amplitude to mean velocity is about $\frac{1}{3}$ and the reduced frequency $k = \omega C/2\overline{U}_{ei}$ is 0.90. Since the reduced frequencies based on the blade chord are of the order of 0.1 for helicopter blades and of the order of 1 for axial compressor blades, these data and those presented in part 4 are within the range of practical reduced frequencies.

Part 4 presents relevant background discussion for this paper. The unsteady-flow terminology and notation used here are the same as in part 4. Exactly the same experimental equipment and wind-tunnel geometry were used in these experiments as those reported in part 4. Since a reader would want to refer to part 4, this information is not reiterated here in the interest of brevity.

## 2. Description of the test flow

The free-stream mean-velocity distributions for this periodic unsteady flow and the $k = 0.61$ flow of Simpson *et al.* (1983) are essentially of the same type as the steady free-stream flow examined by Simpson *et al.* (1981*a*, *b*). Figures 1 and 2 show the streamwise distributions of several parameters associated with the sinusoidal waveform flow discussed here and the steady free-stream flow. All data were obtained at atmospheric pressure and $25 \pm \frac{1}{4}$ °C conditions.

The ensemble-averaged free-stream velocity $\hat{U}_e$ outside the boundary layer can be expressed in terms of its Fourier components $\tilde{U}_{ne}$ as

$$\hat{U}_e = \overline{U}_e \left\{ 1 + \sum_{n=1}^{\infty} \left[ \frac{\tilde{U}_{ne}}{\overline{U}_e} \cos(\omega n t - \phi_{ne}) \right] \right\}. \tag{2.1}$$

The mean free-stream velocity $\overline{U}_e$ obtained along the tunnel centreline using the single-wire probe was repeatable within about 3% over the duration of these experiments, which is slightly greater than the uncertainty of measuring the mean velocity with a hot-wire anemometer ($\pm 2.4\%$). Upstream of 3 m, the first harmonic ratio $\tilde{U}_{1e}/\overline{U}_e$ was about $\frac{1}{3}$ and was repeatable within 2%, while $\phi_{1e}$ only varied 4° or one bin of the oscillation cycle.

Although the variable-angular-velocity rotating-blade damper tended to eliminate higher-harmonic effects, second and third harmonics had amplitudes of about 3.5% of the first harmonic upstream of 3 m and about 5% and 3% respectively downstream. The scatter was about $\pm 15\%$ for $\tilde{U}_{2e}/\overline{U}_e$ and only $\pm 20\%$ for $U_{3e}/\overline{U}_e$ upstream of detachment. Because of the relatively small contribution by these harmonics, there

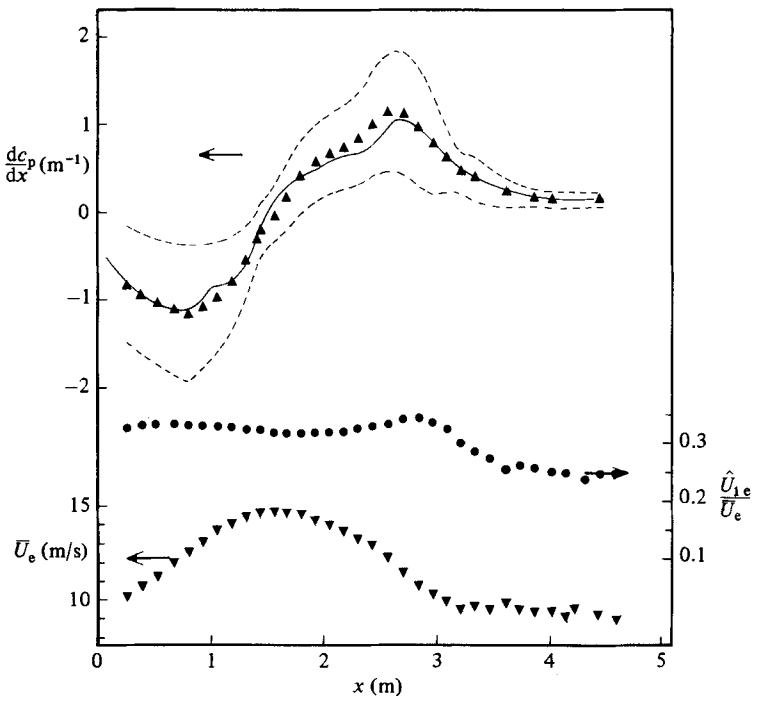


FIGURE 1. Free-stream mean velocity $\overline{U}_e$, amplitude to mean velocity ratio $\hat{U}_{ie}/\overline{U}_e$ and pressure-gradient distributions along the centreline $C_p = 2(P-P_i)/\rho\overline{U}_{ei}^2$; $\overline{U}_{ei} = 10.18$ m/s. Solid line for the steady flow of Simpson *et al.* (1981*a*); dashed lines denote the limits of the unsteady pressure gradient.

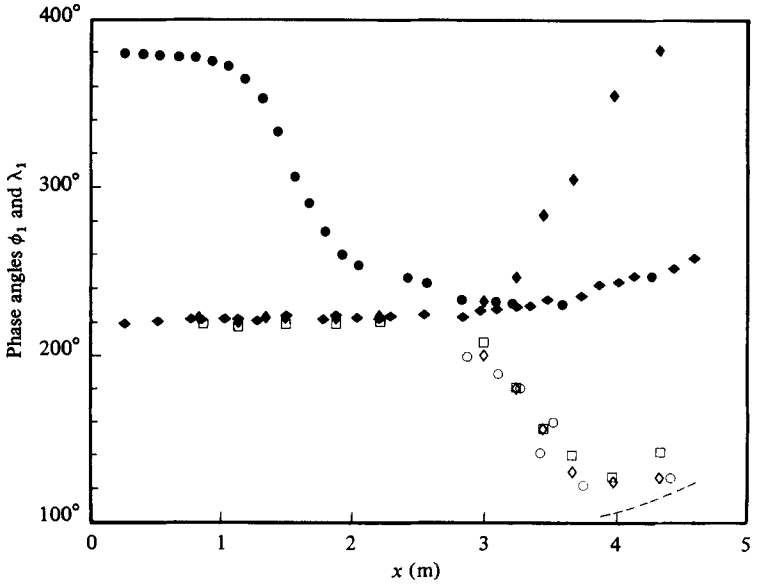


FIGURE 2. Phase angles of first harmonics: ◆, $\phi_{ie}$, free-stream velocity; ●, $\phi_{ie}+180°+\gamma_{ie}$; □, $\phi_{log}$, semilogarithmic velocity region; ◇, $\phi_{1w}$, wall shearing stress; ○, $\lambda_1$, fraction of time flow moves downstream; ◆, $\lambda_{1\tilde{u}^2}$ in semi-log region. Dashed line denotes the phase angle of a pressure-gradient-driven backflow that leads the pressure gradient by 135°.

was relatively greater scatter in $\phi_{2e}$ and $\phi_{3e}$ results, being $\pm 10°$. Fast-Fourier signal analysis revealed that only 0.298 Hz, which is the rotating damper blade frequency, and higher harmonics, produce periodic velocity contributions.

Using this streamwise distribution, the free-stream streamwise pressure gradient can be calculated from the unsteady inviscid equation of motion. The important terms are from the mean and first harmonics, and are given by

$$\frac{1}{\rho}\frac{\mathrm{d}\hat{P}}{\mathrm{d}x} = -[\bar{U}_e\bar{U}_e + \tfrac{1}{2}\tilde{U}_{1e}\tilde{U}'_{1e}] + [(\bar{U}_e\tilde{U}'_{1e} + \tilde{U}_{1e}\bar{U}'_e)^2 + \tilde{U}^2_{1e}(\bar{U}_e\phi'_{1e} - \omega)^2]\cos(\omega t - \phi_{1e} - 180° - \gamma_{1e}), \quad (2.2)$$

where

$$\gamma_{1e} = \arctan\frac{\tilde{U}_{1e}(\bar{U}_e\phi'_{1e} - \omega)}{\bar{U}_e\tilde{U}'_{1e} + \tilde{U}_{1e}\bar{U}'_e}. \quad (2.3)$$

Here primes denote streamwise derivatives. These derivatives were evaluated at a given streamwise location by differentiating the least-squares curve fit of a quadratic model to the five data points nearest that location. The first harmonic contributes a term to the mean-pressure gradient because of the quadratic term in the inviscid equation of motion. Here the mean pressure gradient is about $\frac{19}{18}$ of that due to the mean-velocity term alone upstream of separation.

Figure 1 shows the non-dimensional mean, maximum and minimum pressure gradients $\mathrm{d}C_p/\mathrm{d}x$ along the centreline of the test wall. Here $C_p = 2(P - P_i)/\rho\bar{U}^2_{ei}$, where i denotes the nominal free-stream entrance condition with $U_{ei} = 10.18$ m/s, which is 0.676 of the mean entrance velocity for the unsteady free-stream case of Simpson *et al.* (1983) and the steady free-stream flow of Simpson *et al.* (1981*a*). The mean-pressure gradient agrees with the steady free-stream pressure gradient except near the throat at the 1.5 m location and near the second boundary-layer control location at 2.5 m. The amplitude of the first-harmonic pressure gradient is about 0.55–0.6 of the mean-pressure gradient upstream of detachment and not near the test section throat, as in the case of the high-speed flow of Simpson *et al.* (1983). After detachment the pressure gradient relaxes so that $\mathrm{d}\hat{P}/\mathrm{d}x$ is *never* negative or a favourable pressure gradient. The principal difference between the $\mathrm{d}C_p/\mathrm{d}x$ distributions for the two unsteady flows is that the amplitude of the $\mathrm{d}C_p/\mathrm{d}x$ oscillation for the $k = 0.90$ flow is about $\frac{2}{3}$ of the amplitude for the $k = 0.61$ flow downstream of detachment.

Figure 2 shows $\phi_{1e}$ and the phase angle of the pressure gradient first harmonic, $\phi_{1e} + 180° + \gamma_{1e}$. As in the higher-speed $k = 0.61$ unsteady flow, the first-harmonic pressure gradient strongly lags the local free-stream velocity in the converging section of the tunnel. The lag is considerably lower in the diverging section. After detachment, the oscillatory pressure gradient only slightly leads the velocity oscillation with the onset of pressure-gradient relaxation, i.e. $\phi'_{1e} \geqslant \omega/\bar{U}_e$.

The mean free-stream streamwise turbulent intensity was less than 2 % upstream of separation, and was nearly independent of streamwise position, indicating no strong influence of flow acceleration or deceleration. Fast-Fourier signal analysis showed that, downstream of separation, the increasingly greater free-stream turbulence intensity of up to 4 % contained appreciable contributions at frequencies under 10 Hz. The frequency of passage of large eddies in a turbulent boundary layer can induce irrotational fluctuations in the adjacent free-stream (Phillips 1955). This is believed to be the main source of these greater free-stream turbulence intensities as in the $k = 0.61$ case.

To examine the two-dimensionality of the mean boundary-layer flow, smoke was

introduced only in a spanwise portion of the test-wall boundary layer at a given time. A sheet of laser light produced by a cylindrical lens was used to illuminate the smoke. Upstream of separation, negligible spanwise diffusion of the smoke was observed, indicating no gross flow three-dimensionality. For the steady free-stream flow, velocity profiles at several spanwise locations indicated that the mean velocity was two-dimensional within 1% (Simpson, Chew & Shivaprasad 1980*a*, 1981*a*). Downstream of separation greater spanwise diffusion occurred, so that downstream of 4.4 m no nominally two-dimensional flow remained. Smoke-flow patterns in the sidewall and corner flows were symmetric about the channel centreline, as in the higher-speed steady and unsteady cases.

## 3. Experimental results

Ensemble-averaged velocity profiles were obtained in the unseparated upstream boundary layer and the outer part of the separated flow using a single-wire hot-wire anemometer probe. Only the laser anemometer was used for regions where backflow occurred $\hat{\gamma}_{pu} < 1$. In regions where both laser and hot-wire anemometers produce valid data, the results agreed within experimental uncertainties.

Upstream of 2.6 m, the ensemble-averaged velocity profiles $\hat{U}/\hat{U}_e$ *vs.* $y/\hat{\delta}_{0.99}$ for each phase agree with the mean profile $\overline{U}/\overline{U}_e$ *vs.* $y/\bar{\delta}_{0.99}$ from the outer edge of the viscous sublayer to the free stream. Here $\delta_{0.99}$ is the location from the test wall where $\overline{U}/\overline{U}_e$ is 0.99. The quantity $\bar{\delta}_{0.99}$ is the cycle average of $\hat{\delta}_{0.99}$, which is the location from the wall where $\hat{U}/\hat{U}_e$ is 0.99. In general, $\delta_{0.99}$ is different from $\bar{\delta}_{0.99}$, since the location on an averaged profile is not the same as the average of locations on ensemble-averaged profiles.

Figure 2 shows the first-harmonic phase angles $\phi_{1e}$ and $\phi_{1\log}$ for the free-stream velocity and the ensemble-averaged velocity in the semilogarithmic region. Upstream of 2.6 m, $\phi_{1\log}$ is about 2°–3° lower than $\phi_{1e}$, as in the $k = 0.61$ case. This difference is not due to experimental uncertainty. All these data show a smooth gradual increase of $\phi_1$ from the semilogarithmic region to the free stream. As in the $k = 0.61$ case, the ratio of the first harmonic to the mean velocity $\tilde{U}_1/\overline{U}$ was closely equal to $\tilde{U}_{1e}/\overline{U}_e$ from the semilogarithmic region to the outer edge of the boundary layer at these upstream locations, as shown in figure 3. As in the free stream, the second and third harmonics had amplitudes of about 3.5% of the first harmonic. Figure 2 shows that the phase angle $\lambda_1$ for $(\widehat{u^2})_1$ in the semilogarithmic region is in phase with $\phi_{1\log}$.

Upstream of 2 m, the mean-skin-friction results from the surface hot-wire skin friction gauge agree with Preston-tube and Ludwieg–Tillman results for a steady flow with the same free-stream velocity distribution. As in the $k = 0.61$ case, $\tilde{\tau}_{w1}/\bar{\tau}_w$ is nearly constant to within about $\pm 10\%$, as shown on the ordinate of figure 3. The phase angle for the wall-shearing stress $\phi_{1w}$ is shown in figure 2. The phase angle for $(\tau_w'^2)_1$ is closely equal to $\phi_{1w}$.

Upstream of 2.6 m, $\phi_1$ in the viscous sublayer is no more than 5° lower than $\phi_1$ in the semilogarithmic region. The nearest wall data and $\phi_{1w}$ from the surface hot-wire data indicate that $\phi_1$ approaches a value near $\phi_{1\log}$ at the wall, as in the $k = 0.61$ case. As discussed in appendix B of part 4 (Simpson *et al.* 1983), this measured phase lead of $\tilde{U}_1$ near the wall in the viscous sublayer is apparently due to very small oscillations of the hot-wire probe relative to the test wall at the oscillation frequency. The measured phase lead was as much as 50° for the $k = 0.61$ flow. It is much lower in the present flow because the pressure oscillations are about a third of those in the $k = 0.61$ flow, resulting in much smaller wall and probe oscillations.

Figure 4 shows mean-velocity profiles near detachment and downstream. Note the

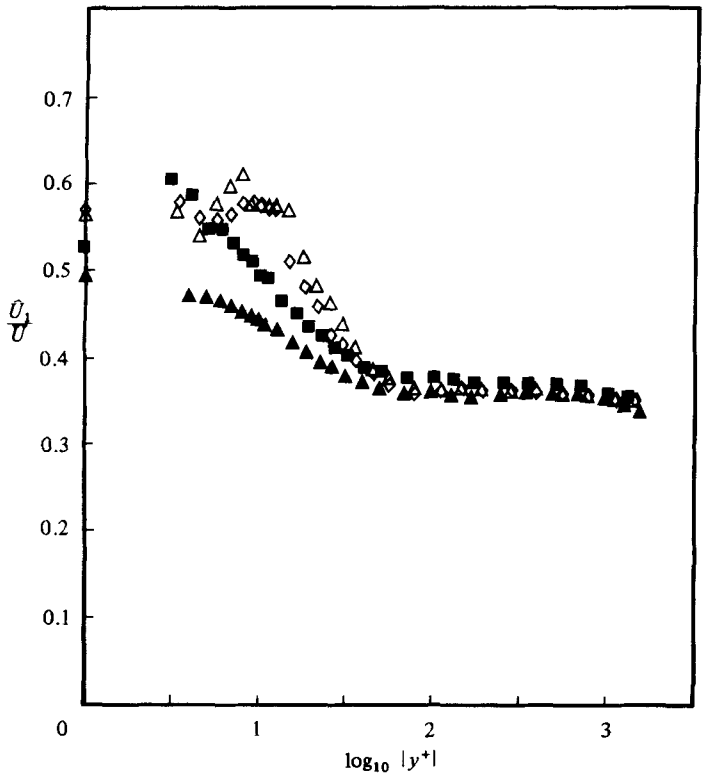


FIGURE 3. $\tilde{U}_1/\overline{U}$ *vs.* $y^+$ upstream of detachment from hot-wire data: ◇, 1.14 m; △, 1.48 m; ■, 1.86 m; ▲, 2.21 m. Values of $\tilde{\tau}_{w1}/\overline{\tau}_w$ from surface skin-friction gauge shown on ordinate.

| $x$ (m) | $\delta^*$ (mm) | $\theta$ (mm) | $\delta_{0.99}$ (mm) | $\overline{U}_e$ (m/s) |
|---|---|---|---|---|
| 3.01 | 38.17 | 16.41 | 118.87 | 10.05 |
| 3.25 | 108.44 | 20.23 | 163.83 | 9.79 |
| 3.45 | 106.17 | 23.10 | 219.71 | 9.58 |
| 3.67 | 151.00 | 23.26 | 292.10 | 9.20 |
| 3.99 | 210.68 | 20.82 | 359.4 | 9.15 |
| 4.34 | 266.78 | 20.71 | 406.4 | 8.97 |

TABLE 1. Parameters for the mean-velocity profiles

| $x$ (m) | $\tilde{U}_{ei}/\overline{U}_e$ | $\phi_{ei}$ | $\tilde{U}_{e2}/\overline{U}_e$ | $\phi_{e2}$ |
|---|---|---|---|---|
| 3.01 | 0.328 | 227.8° | 0.006 | 51.7° |
| 3.25 | 0.293 | 232.7° | 0.011 | 48.0° |
| 3.45 | 0.274 | 237.1° | 0.014 | 66.5° |
| 3.67 | 0.276 | 242.6° | 0.012 | 52.6° |
| 3.99 | 0.250 | 247.9° | 0.013 | 102.6° |
| 4.34 | 0.250 | 255.8° | 0.010 | 169.3° |

TABLE 2. First- and second-harmonic velocity parameters outside the turbulent shear layer

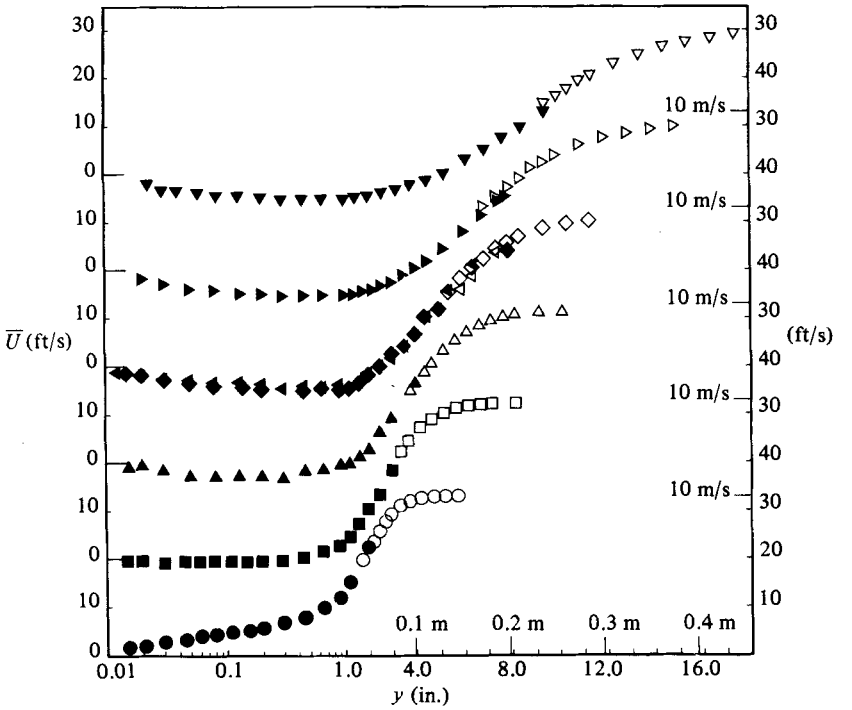


FIGURE 4. Mean velocity $\overline{U}$ *vs.* $y$ near detachment and downstream; solid symbols, laser anemometer data; open symbols, hot-wire anemometer data: ○, 3.00 m; □, 3.25 m; △, 3.45 m; ◇, 3.67 m; ▷, 3.98 m; ▽, 4.34 m. Note displaced ordinates and the log-linear abscissa.

| $x$ (m) | $\bar{\delta}^*$ (mm) | $\tilde{\delta}_1^*$ (mm) | $\phi_{\delta^*1}$ | $\tilde{\delta}_2^*$ (mm) | $\phi_{\delta^*2}$ | $\tilde{\delta}_3$ (mm) | $\phi_{\delta^*3}$ | $\tilde{\delta}_4$ (mm) | $\phi_{\delta^*4}$ |
|---|---|---|---|---|---|---|---|---|---|
| 3.01 | 41.40 | 20.83 | 29.9° | 5.92 | 68.4° | 1.64 | 78.4° | 0.40 | 118° |
| 3.25 | 76.89 | 35.31 | 30.7° | 7.42 | 68.6° | 1.94 | 82.6° | 0.32 | 147° |
| 3.45 | 111.4 | 42.93 | 31.7° | 6.99 | 76.4° | 2.09 | 97.0° | 0.85 | 264° |
| 3.67 | 157.1 | 55.63 | 31.1° | 7.24 | 77.6° | 2.26 | 82.9° | 0.65 | 321° |
| 3.99 | 216.8 | 64.01 | 28.7° | 8.03 | 89.7° | 1.59 | 104.0° | 1.22 | 23.9° |
| 4.34 | 273.0 | 66.80 | 24.4° | 7.24 | 87.7° | 1.13 | 2.64° | 1.89 | 87.2° |
| $x$ (m) | $\bar{\theta}$ (mm) | $\tilde{\theta}_1$ (mm) | $\phi_{\theta1}$ | $\tilde{\theta}_2$ (mm) | $\phi_{\theta2}$ | $\tilde{\theta}_3$ (mm) | $\phi_{\theta3}$ | $\tilde{\theta}_4$ (mm) | $\phi_{\theta4}$ |
| 3.01 | 14.48 | 1.308 | 41.6° | 0.95 | 192° | 0.64 | 238° | 0.30 | 263.0° |
| 3.25 | 15.57 | 3.708 | 167.0° | 2.59 | 187° | 1.25 | 231° | 0.27 | 305.0° |
| 3.45 | 18.08 | 4.394 | 121.0° | 3.25 | 173° | 1.11 | 252° | 0.31 | 66.5° |
| 3.67 | 16.15 | 11.02 | 153.0° | 6.65 | 194° | 1.92 | 252° | 0.28 | 50.2° |
| 3.99 | 13.23 | 21.16 | 157.0° | 10.74 | 223° | 2.43 | 294° | 0.61 | 69.9° |
| 4.34 | 13.31 | 31.24 | 177.0° | 16.28 | 252° | 2.79 | 313° | 0.52 | 210.0° |

$$\delta^* = \bar{\delta}^* + \sum_{n=1}^{4} \delta^* \cos(n\omega t - \phi_{\delta^* n}) \quad \theta = \bar{\theta} + \sum_{n=1}^{4} \tilde{\theta}_n \cos(n\omega t - \phi_{\theta n})$$

TABLE 3. Parameters for the first four harmonics of the displacement and momentum thicknesses of ensemble-averaged profiles

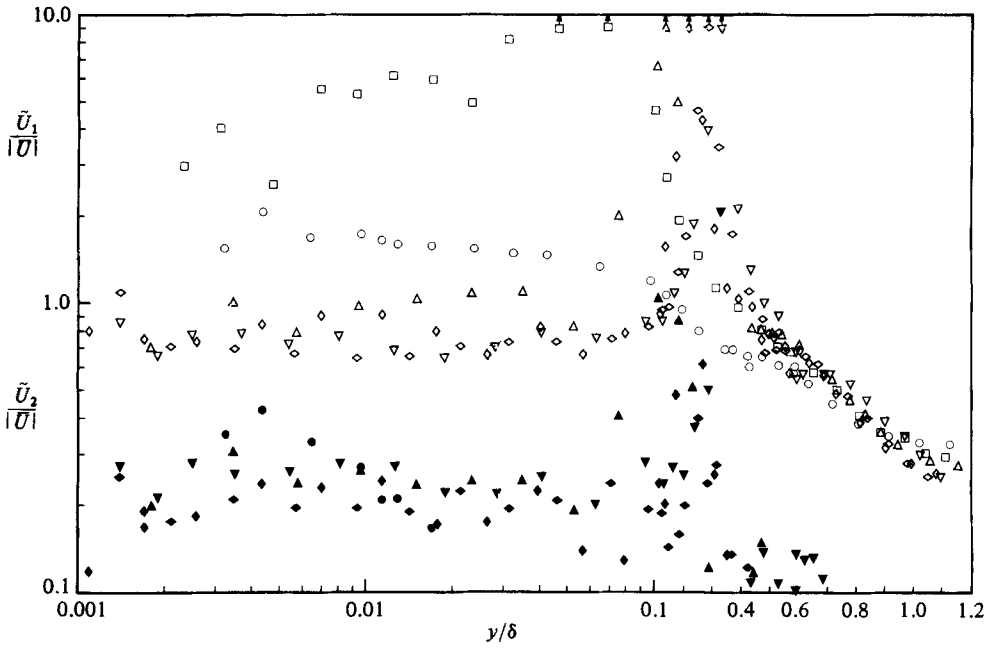


FIGURE 5. Ratios of velocity amplitude to absolute mean-velocity profiles near detachment and downstream. $\tilde{U}_1/|\overline{U}|$ *vs.* $y/\delta$, open symbols; $\tilde{U}_2/|\overline{U}|$ *vs.* $y/\delta$, solid symbols: ○, 3.00 m; □, 3.25 m; △, 3.45 m; ◇, 3.67 m; ◇, 3.98 m; ▽, 4.34 m. Note the log-linear abscissa.

overlap region for each profile where both laser and hot-wire anemometer data are valid. Tables 1–3 present parameter values for these data. At the 3.00 m location, near-wall backflow only occurs in a small fraction of the cycle, as discussed below, so a distinct semilogarithmic velocity profile can be observed in figure 4. At 3.25 m, $\overline{U}$ is nearly zero near the wall. Downstream, the mean backflow profiles have shapes similar to those for the $k = 0.61$ unsteady flow and the steady flow of Simpson *et al.* (1981*a*), as discussed below.

Figure 5 shows the ratio of velocity amplitude to absolute mean velocity for the first two harmonics. At 3.00 m, $\tilde{U}_1/|\overline{U}|$ is nearly constant in the semilogarithmic mean-profile region, and approaches the free-stream value in the outer region. This behaviour is consistent with the data for the $k = 0.61$ flow near detachment, with $\tilde{U}_1/|\overline{U}|$ being much higher in the semilogarithmic region than in the free stream. Naturally, as $\overline{U}$ approaches zero, $\tilde{U}_1/|\overline{U}|$ becomes very large, as for the data at 3.25 m.

For the downstream locations with mean backflow, figure 5 shows that $\tilde{U}_1/|\overline{U}|$ is nearly constant in the mean backflow region ($y/\delta < 0.1$) at each location. As in the $k = 0.61$ case, these $\overline{U}_1/|U|$ values decrease from about 1.0 to 0.7 as one proceeds downstream. Within the inner 40% of the mean-flow layer, $\overline{U}$ approaches zero, so that large $\tilde{U}_1/|\overline{U}|$ values occur. In the outer half of the layer, the $\tilde{U}_1/|\overline{U}|$ profile is nearly the same at each location.

Downstream of 2.6 m, where backflow occurs at least some of the time, $\phi_{1\log}$ is progressively less than upstream values while $\phi_{1c}$ increases as shown in figure 2. Figure 6 shows that $\phi_1$ near the wall is almost constant at each streamwise location.

The second-harmonic to mean ratio $\tilde{U}_2/|\overline{U}|$ also has nearly uniform values of 0.2–0.3 in the inner 0.1 of the shear layer, as shown in figure 5. In the other region past where

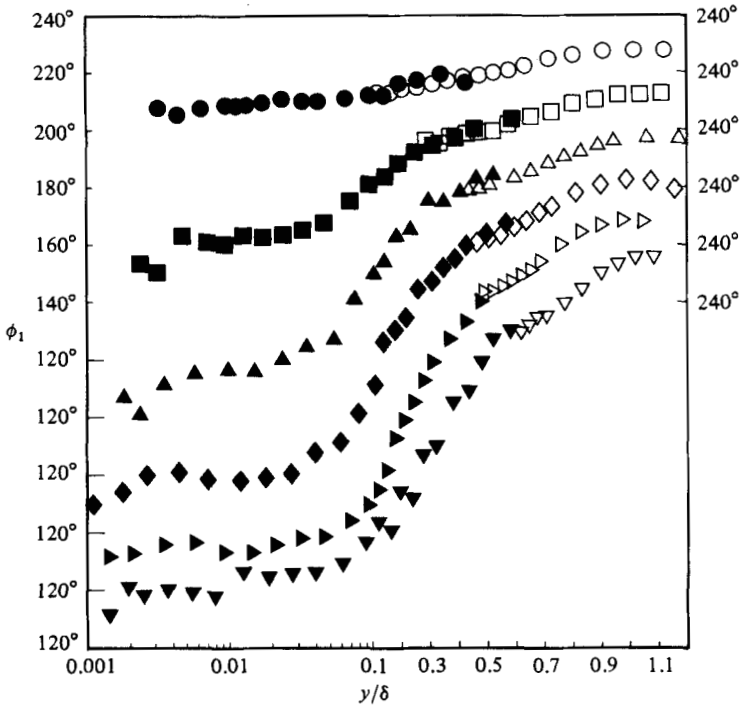


FIGURE 6. Phase angle $\phi_1$ for the first harmonic of $\hat{U}$. Legend same as in figure 5. Note displaced ordinates and the log–linear abscissa.

$\overline{U}$ is zero, $\tilde{U}_2/\tilde{U}$ decreases to the value of 0.015 or less in the free stream. The phase angle $\phi_2$ is more scattered than $\phi_1$ in the inner 0.1 of the shear layer and has values of $100° \pm 20°$, $105° \pm 10°$, $155° \pm 20°$, $190° \pm 15°$, $230° \pm 10°$ and $260° \pm 15°$ for the streamwise locations shown in figure 6 as one proceeds downstream. In this near-wall region, $\tilde{U}_3/|\overline{U}|$ is less than about half of $\tilde{U}_2/|\overline{U}|$ upstream of 3.67 m and less than about $\frac{1}{4}$ of $\tilde{U}_2/|\overline{U}|$ at the last two locations. The phase angle $\phi_3$ is more scattered because of the uncertainty associated with small amplitudes and has values of $195° \pm 10°$, $230° \pm 10°$, $270° \pm 25°$, $240° \pm 30°$, $220° \pm 30°$, and $150° \pm 75°$ respectively.

The only turbulence quantity measured was $\widehat{u^2}$. Profiles of $(\widehat{u^2})^{\frac{1}{2}}/\overline{U}_e$ *vs.* $y/\delta$ agreed to within experimental uncertainties with the $k = 0.61$ flow and the steady-flow data for the same values of $\overline{\gamma}_{pu}$ near the wall. The $y$-location of the maximum $\overline{u^2}$ is within 10 % of $\delta^*$ for a given profile. Figure 2 shows that the phase angle for $\widetilde{u_1^2}$ in the backflow near the wall is progressively greater than the free-stream velocity downstream of detachment. At the location of maximum $\overline{u^2}$ across the shear layer, the phase angle for $\widetilde{u_1^2}$ is progressively greater than the phase angle for $\tilde{U}_1$ downstream of detachment, having values of 245°, 258°, 260°, 268°, 295° and 280° with an uncertainty of $\pm 10°$ respectively. This type of behaviour is the same as for the $k = 0.61$ flow. These results indicate that the turbulence structure progressively lags the ensemble-averaged flow oscillation downstream of detachment.

Figure 7 shows profiles of time-averaged values of $\overline{\gamma}_{pu}$ of the fraction of time that the flow moves downstream that were measured by the laser anemometer. As in the steady flows of Simpson, Strickland & Barr (1977) and Simpson *et al.* (1981*a*), $\overline{\gamma}_{pu}$ is nearly constant in the mean backflow region within the inner 10 % of the detached

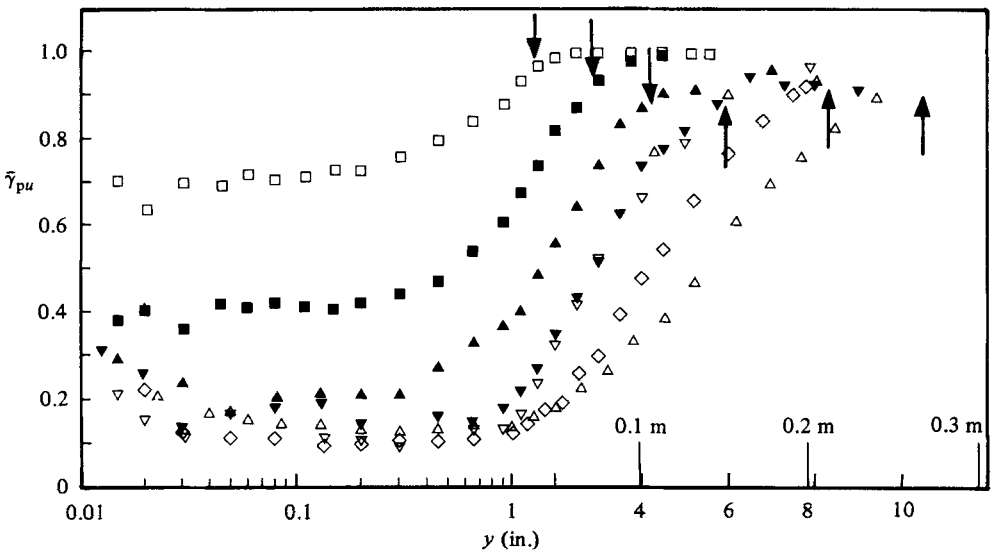


FIGURE 7. Profiles of time-averaged fraction of time that the flow moves downstream $\bar{\gamma}_{pu}$: □, 3.00 m; ■, 3.25 m; ▲, 3.45 m; ▽, ▼, 3.67 m; ◇, 3.98 m; △, 4.34 m. Arrows from left to right denote the locations of $\delta^*$ for the six streamwise locations respectively. Note the log-linear abscissa.

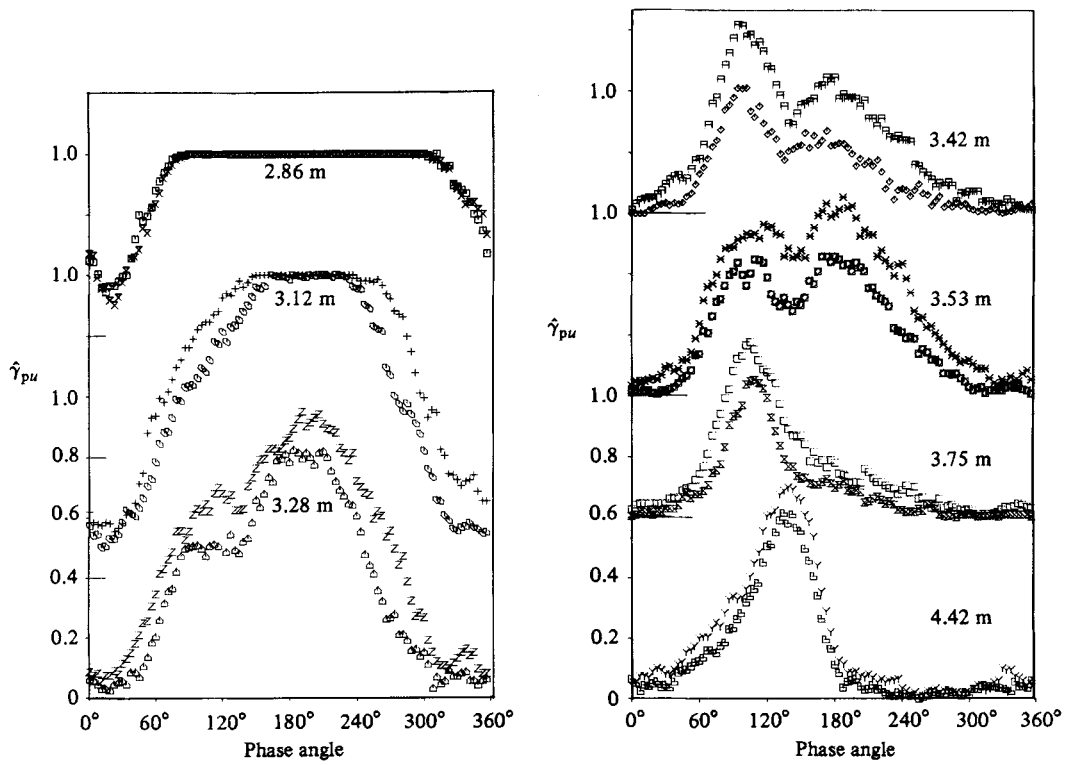


FIGURE 8. Phase-averaged $\hat{\gamma}_{pu}$ measured 1.22 mm from the wall *vs.* $\omega t$ by the thermal tuft with two orientations. Higher set of data at each streamwise location obtained by the same thermal-tuft orientation.

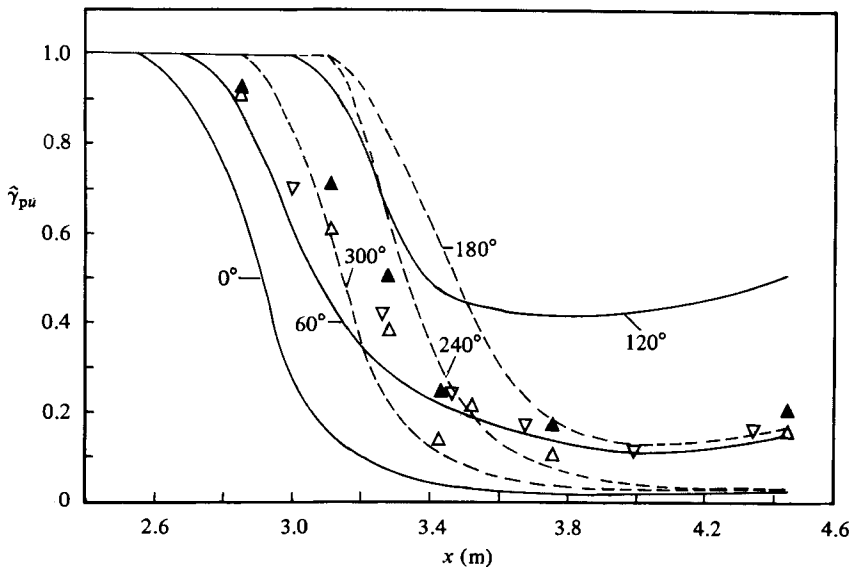


FIGURE 9. Phase-averaged $\hat{\gamma}_{pu}$ at 1.22 mm *vs.* $X$ for different phases of a cycle shown by lines. Cycle averaged $\overline{\gamma}_{pu}$ values shown by symbols. Thermal tuft: △, one orientation; ▲, reversed orientation. Laser anemometer: ▽.

shear layer. $\overline{\gamma}_{pu}$ approaches unity near the maximum $\overline{u^2}$ location or near the $\delta^*$ location, which is noted for each profile on figure 7. The shape of these distributions follow approximately the distribution given by Simpson *et al.* (1977):

$$\frac{\overline{\gamma}_{pu}-\overline{\gamma}_{pu\,\min}}{1-\overline{\gamma}_{pu\,\min}} = g\left(\frac{y}{M}\right),$$

where $\overline{\gamma}_{pu\,\min}$ is the near-wall minimum value and $M$ is the distance from the wall to where $\overline{u^2}$ is a maximum.

Figure 8 shows the ensemble-averaged values of thermal-tuft data of the fraction of time that the flow moves downstream $\hat{\gamma}_{pu}$ at 1.22 mm from the wall for a cycle at several streamwise locations. At each location data were determined for two orientations of the thermal tuft of Shivaprasad & Simpson (1982). At all locations both in this flow and the $k = 0.61$ case, data obtained at the second orientation were higher than LDV results as noted by Shivaprasad & Simpson.

Nevertheless, this figure shows that $\hat{\gamma}_{pu}$ *vs.* $\omega t$ near the wall has different features than those for the $k = 0.61$ flow. Here double peaks occur between 3.28 m and 3.53 m, while no double peaks occur in the $k = 0.61$ flow. Laser-anemometer $\hat{\gamma}_{pu}$ data 1.2 mm from the wall at 3.25 m and 3.45 m also show this double-peaked behaviour. In both types of data a local minimum between the peaks occurs at 135°. At far downstream locations both flows have nearly constant low values of $\hat{\gamma}_{pu\,\min}$ from about 40° before the peak free-stream velocity till about 140° after the peak. While $\hat{U}$ and $\widehat{u^2}$ have nearly sinusoidal variations near the wall, figure 8 shows that $\hat{\gamma}_{pu\,\min}$ is not described by a single harmonic variation. Still, figure 2 shows that the phase angle $\lambda_1$ for the first-harmonic $\tilde{\gamma}_{pu\,1}$ near the wall is nearly in phase with $\tilde{U}_1$ downstream of 3 m, as was the case with the $k = 0.61$ flow.

Figure 9 presents the cycle-averaged or time-averaged values of $\overline{\gamma}_{pu\,\min}$ near the wall and $\hat{\gamma}_{pu\,\min}$ *vs.* $x$ for various phases of the oscillation cycle. Note the agreement between cycle-averaged laser-anemometer and thermal-tuft results. As in the

$k = 0.61$ flow, there is hysteresis in the unsteady separated flow. When the free-stream velocity increases between 40° to 120° of a cycle, the location where $\hat{\gamma}_{pu\,\min}$ is less than one moves downstream and $\hat{\gamma}_{pu\,\min}$ increases at all downstream locations as backflow fluid is washed downstream and the shear-layer thickness decreases significantly. Since the adverse pressure gradient is almost in phase with the free-stream velocity, it also increases and causes progressively greater backflow at downstream locations as the free-stream flow increases between 120° and 180°, while $\hat{\gamma}_{pu\,\min}$ remains high upstream. After backflow occurs a large fraction of time at downstream locations, the location where $\hat{\gamma}_{pu}$ is less than unity moves upstream as the free-stream velocity decreases from 240° back to the minimum near 40°. As discussed below, there are distinct differences in this flow behaviour for the two unsteady flows.

## 4. Discussion

Upstream of 2.6 m, the mean-velocity profiles in the semilogarithmic region agree with the steady-flow equation

$$U^+ = \frac{1}{\kappa}\ln|y^+| + C \tag{4.1}$$

with $\kappa = 0.41$ and $C = 5.0$ when mean surface-shearing stresses from the surface hot-wire gauge are used. Both Simpson *et al.* (1981*a*) for steady flow and Simpson *et al.* (1983) for the $k = 0.61$ unsteady flow found this equation to hold upstream of any flow reversal. As proved by Simpson (1977), and supported by the $k = 0.61$ data, the phase-angle variation of the ensemble-averaged oscillation velocity data is zero within the semilogarithmic region. As in the $k = 0.61$ case, the ensemble-averaged velocity profiles upstream of any flow reversal for this low-frequency moderate-amplitude oscillation experiment are satisfied by (4.1) at each phase of a cycle within experimental uncertainties. Conversely, when (4.1) is assumed to hold at each phase of a cycle, the calculated values of $\tilde{U}_1/\overline{U}$ in the semilogarithmic region agree with experimental values shown in figure 3, as in the $k = 0.61$ case. Also, the phase angle in the semilogarithmic region is the same as for the wall shearing stress, as shown in figure 2.

The differential streamwise-momentum equation also requires that the wall shearing-stress amplitude and phase be the same as the shear stress in the semilogarithmic region at oscillation frequencies low compared with the turbulence-energy-containing frequencies. Davis (1974) used a dynamic model to predict the oscillatory turbulent Reynolds stresses outside the viscous sublayer:

$$\tilde{\tau} = 2\kappa(-\overline{uv})^{\frac{1}{2}} y \frac{\partial \tilde{U}}{\partial y}. \tag{4.2}$$

Since (4.1) implies that

$$\bar{\tau} = -\overline{uv} = \left(\kappa y \frac{\partial \overline{U}}{\partial y}\right)^2, \tag{4.3}$$

then

$$\frac{\tilde{\tau}_1}{\bar{\tau}} = \frac{\tilde{\tau}_{1w}}{\bar{\tau}_w} = 2\frac{\partial \tilde{U}_1/\partial y}{\partial \overline{U}/\partial y} \tag{4.4}$$

for the semilogarithmic region. At the wall

$$\frac{\tilde{\tau}_{1w}}{\bar{\tau}_w} = \left.\frac{\partial \tilde{U}_1/\partial y}{\partial \overline{U}/\partial y}\right|_w, \tag{4.5}$$

because the wall shearing stress is entirely determined by viscosity and the wall velocity gradient. Note that these equations imply that the ratio of oscillatory velocity gradient to mean-velocity gradient at the wall is twice that of the semilogarithmic region. Since $\tilde{U}_1/\bar{U}$ is nearly constant in the semilogarithmic region, as has been observed by Simpson, Chew & Shivaprasad (1980*b*) for the $k = 0.61$ flow, and is shown in figure 3 for this flow, then these equations imply that

$$\frac{\tilde{\tau}_{w1}}{\bar{\tau}_w} = \frac{2\tilde{U}_1}{\bar{U}}\bigg|_{\log}. \tag{4.6}$$

This result was satisfied by the $k = 0.61$ flow data within experimental uncertainties in figure 21 of part 4, with the measured $\tilde{\tau}_{w1}/\bar{\tau}_w$ values being 10% higher. Figure 3 shows that the measured $\tilde{\tau}_{w1}/\bar{\tau}_w$ values are about 20% below the 0.7 value predicted by (4.6). As shown by Simpson *et al.* (1983) for the $k = 0.61$ flow, the quasisteady analysis of Houdeville & Cousteix (1979) and Cousteix, Houdeville & Javelle (1981) predicts values for $\tilde{\tau}_{w1}/\bar{\tau}_w$ close to those predicted by (4.6) for this flow.

As in the $k = 0.61$ flow, the Perry & Schofield (1973) mean-velocity-profile correlations for strong-adverse-pressure-gradient turbulent boundary layers were satisfied by ensemble-averaged velocity profiles for phases of the cycle when $\hat{\gamma}_{pu}$ was not less than unity. As shown in part 4, when $\hat{\gamma}_{pu} < 1$, the near-wall portion of the Perry & Schofield correlations breaks down first. The outer-region mean-velocity-profile correlation appears to remain valid until $\hat{\gamma}_{pu} \lesssim 0.8$.

Even though large phase variations exist through the downstream detached shear flow and the flow at all phases is not quasi-steady, phase-averaged profiles for a given value of $\hat{\gamma}_{pu\,min}$ are compared in figure 10 with the steady detaching-flow profiles of Simpson *et al.* (1981*a*) at the same $\gamma_{pu\,min}$ value. The basis for this comparison is the steady-flow result that the velocity-profile shape factor $H$ is closely related to $\gamma_{pu\,min}$, as discussed by Simpson *et al.* (1983). For each $\hat{\gamma}_{pu\,min}$ value shown, there is good agreement of $\hat{U}/\hat{U}_e$ *vs.* $y/\delta^*$ phase-averaged profiles with steady-flow profiles when $\partial\hat{\gamma}_{pu\,min}/\partial t < 0$. Since the pressure gradient is almost in phase with $\hat{U}_e$ in the detached-flow zone, $\partial(\mathrm{d}\hat{P}/\mathrm{d}x)/\partial t < 0$ during these phases.

This result is slightly different from that for the $k = 0.61$ flow. In that flow there was good agreement of $\hat{U}/\hat{U}_e$ *vs.* $y/\delta^*$ phase-averaged profiles with steady profiles when $\partial\hat{U}_e/\partial t < 0$ and $\partial\hat{\gamma}_{pu\,min}/\partial t \leqslant 0$. In that case, variations from the steady profiles at a given $\hat{\gamma}_{pu\,min}$ were much smaller than in the current $k = 0.90$ case. A reanalysis of the $k = 0.61$ case revealed that, with exception of a few data points in a few profiles, there was also good agreement between steady and phase-averaged profiles when $\partial\hat{\gamma}_{pu}/\partial t < 0$. As in the $k = 0.61$ case, mean profiles of $\bar{U}/\bar{U}_e$ *vs.* $y/\delta$ do not compare well with steady free-stream results for the same $\bar{\gamma}_{pu\,min}$.

The mean backflow for the $k = 0.61$ flow scales on the maximum negative mean velocity $|\bar{U}_N|$ and its distance $\bar{N}$ from the wall. Figure 11 shows this to be the case too for this flow. The line shown in this figure is an empirical data fit from the steady flow for the semilogarithmic overlap region between the viscous wall layer and the large-scaled outer region. Simpson (1983) has shown that

$$\frac{U}{|U_N|} = 0.3\left(\frac{y}{N} - \ln\left(\frac{y}{N}\right) - 1\right) - 1 \tag{4.7}$$

fits steady free-stream data of Simpson *et al.* (1981*a*), Westphal (1982) and Hastings & Moreton (1982) for $0.02 < y/N < 1$. Since the phase angle of the periodic backflow velocity and $\tilde{U}_1/|\bar{U}|$ are nearly independent of $y$ for this near-wall region, the ensemble-averaged backflow in this region behaves like a quasisteady flow when normalized on $|\hat{U}_N|$ and $\hat{N}$, as was observed for the $k = 0.61$ flow.

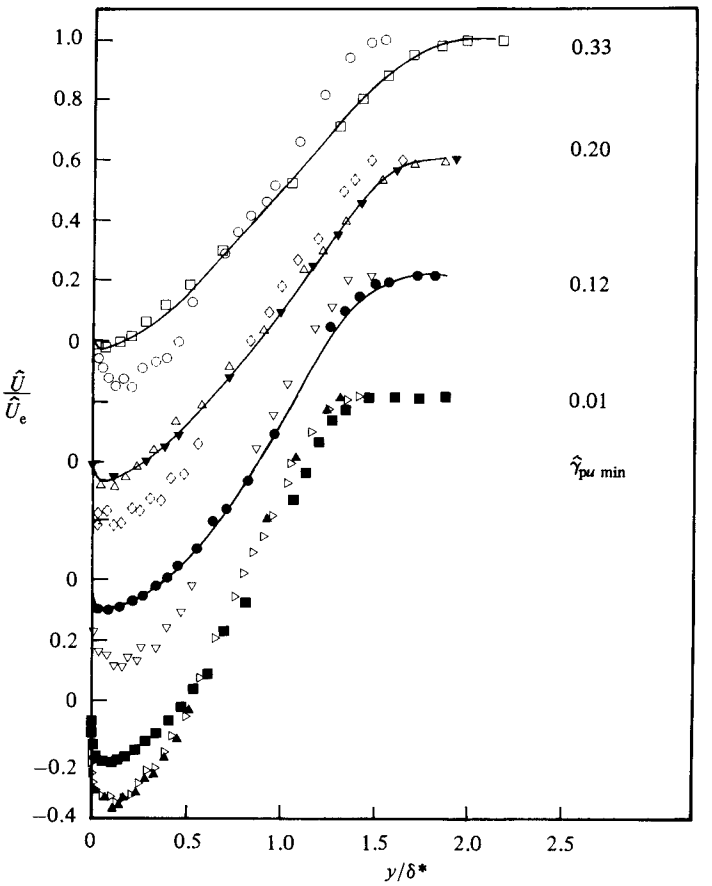


FIGURE 10. Phase-averaged velocity profiles $\hat{U}/\hat{U}_e$ *vs.* $y/\delta^*$ for several values of $\hat{\gamma}_{pu\,min}$. Solid lines denote profiles from the steady flow of Simpson *et al.* (1981*a*) at the $\gamma_{pu\,min}$ value. Note displaced ordinates. Conditions for each profile are as below.

| | $\hat{\gamma}_{pu\,min}$ | $\partial\hat{\gamma}_{pu\,min}/\partial t$ | $X$ | Phase angle | $\hat{H}$ |
|---|---|---|---|---|---|
| □ | 0.33 | $< 0$ | 3.25 m | 281° | 3.78 |
| ○ | 0.33 | $> 0$ | 3.67 m | 82° | 7.37 |
| △ | 0.20 | $< 0$ | 3.25 m | 304° | 4.66 |
| ▼ | 0.20 | $< 0$ | 4.34 m | 176° | 5.31 |
| ◇ | 0.20 | $\approx 0$ | 4.34 m | 79° | 49.74 |
| ● | 0.12 | $< 0$ | 3.98 m | 195° | 7.58 |
| ▽ | $\approx 0.12$ | $> 0$ | 4.34 m | 60° | −21.11 |
| ■ | $\approx 0.01$ | $< 0$ | 3.98 m | 274° | 17.75 |
| ▷ | $\approx 0.01$ | $\leqslant 0$ | 3.98 m | 352° | −26.57 |
| ▲ | $\approx 0.01$ | $> 0$ | 4.34 m | 11° | −12.18 |

Another similarity with this earlier experiment is that the phase angle $\phi_1$ in the backflow has a progressively greater phase lead as one proceeds downstream. Using the unsteady vorticity equation and assuming that the nearest wall flow is governed by viscosity and the oscillating and mean pressure gradient, Simpson *et al.* (1983) showed that the near-wall velocity oscillation leads the pressure-gradient oscillation by 135°. Figure 2 shows that $\phi_1$ near the wall approaches this 135° lead asymptotically.

Figure 12 shows $\hat{\gamma}_{pu\,min}$ *vs.* $(\hat{H}-1)/\hat{H}$ or $\hat{h}$ for this flow. Simpson *et al.* (1983) showed

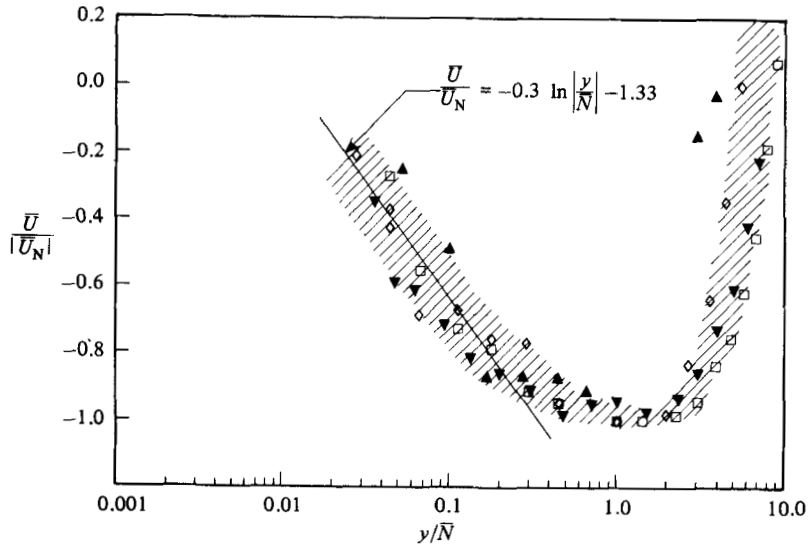


FIGURE 11. Normalized backflow mean-velocity profiles for this unsteady flow: ▲, 3.45 m; □, 3.67 m; ◇, 3.98 m; ▼, 4.34 m. Shaded region denotes data from the steady free-stream flow of Simpson *et al.* (1981*a*) and the $k = 0.61$ unsteady-flow data of Simpson *et al.* (1983).

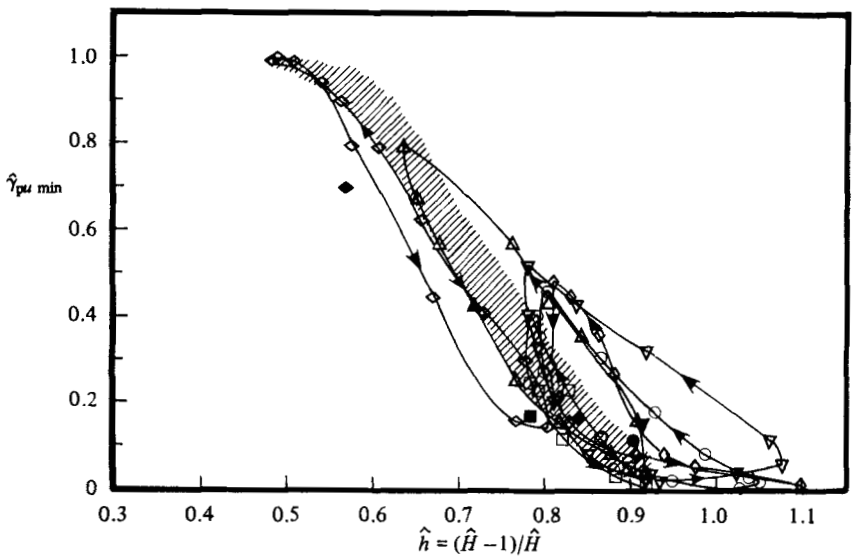


FIGURE 12. $\hat{\gamma}_{pu\,min}$ *vs.* $\hat{h}$ for the current unsteady flow from LDV data: ◇, 3.00 m; △, 3.25 m; □, 3.45 m; ◇, 3.67 m; ○, 3.98 m; ▽, 4.34 m. Solid lines form hysteresis loops for data at a given streamwise position. Shaded region denotes steady-flow results presented by Simpson *et al.* (1983). Solid symbols denote mean unsteady-flow results.

that the steady-flow results of Simpson *et al.* (1981*a*) occurred in the shaded region of this plot and that the $k = 0.61$ flow results largely fell in this region. When $\hat{\gamma}_{pu\,min}$ reaches its cycle maximum value it is above the shaded region except for the two upstream locations where $\hat{\gamma}_{pu\,min} > 0.5$ – a substantial part of the cycle. In general the ensemble-averaged data agree with the steady-flow results when $\partial\gamma_{pu\,min}/\partial t < 0$. At the last three locations shown, $\hat{\gamma}_{pu\,min}$ first decreases, while $\hat{h}$ remains nearly constant. $\hat{\gamma}_{pu\,min}$ falls to much lower values than encountered in the steady or the

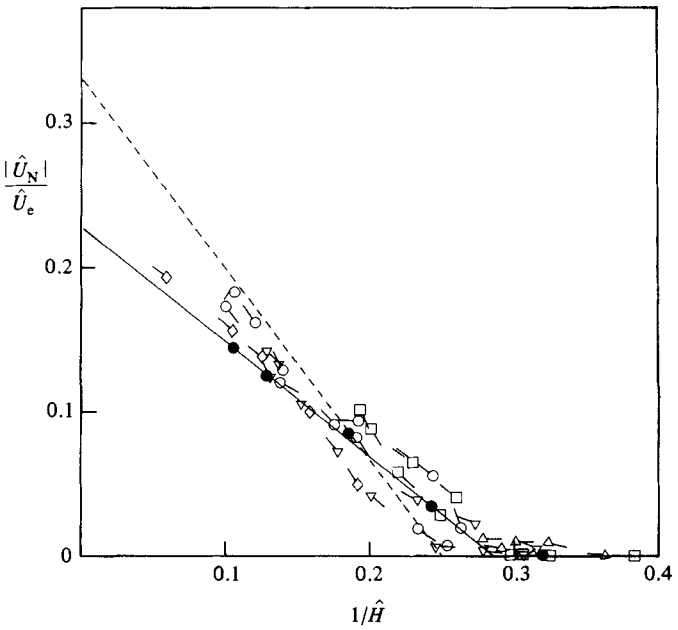


FIGURE 13. $|\hat{U}_N|\ \hat{U}_e$ *vs.* $1/\hat{H}$ for the $k = 0.61$ flow of Simpson *et al.* (1983). Solid line given by (4.8); dashed line by (4.10). Solid symbols denote steady-flow data. Leader on each symbol points in the local direction of a hysteresis loop for a given streamwise location: △, 3.23 m; □, 3.52 m; ▽, 3.68 m; ○, 3.97 m; ◇, 4.34 m.

$k = 0.61$ flows, and $\hat{h}$-values exceed unity. When $\partial\gamma_{pu\,\min}/\partial t > 0$, the counterclockwise hysteresis loops rise substantially above the steady results. These loops are much larger than for the $k = 0.61$ flow.

This agreement of steady-flow results and ensemble-averaged unsteady results when $\partial\gamma_{pu\,\min}/\partial t < 0$ is further illustrated in figures 13–16. The influence of reduced frequency can be seen clearly in these plots. Figure 13 presents the normalized maximum backflow velocity $|\hat{U}_N|/\hat{U}_e$ *vs.* $1/\hat{H}$ for the $k = 0.61$ flow and the steady flow. The solid line is a good fit of the steady-case data, being given by

$$\frac{|\hat{U}_N|}{U_N} = 0.807\left(1-\frac{1}{\hat{H}}\right)-0.577. \tag{4.8}$$

The ensemble-averaged profiles for phases when $\partial\gamma_{pu\,\min}/\partial t \geqslant 0$ are more rounded near the wall and near the free stream for a given $|\hat{U}_N|/\hat{U}_e$ value, as observed in figure 10. If we let a rounded profile be given crudely by

$$\frac{\hat{U}}{\hat{U}_e} = \frac{1}{2}\left(1-\frac{|\hat{U}_N|}{\hat{U}_e}\right)-\frac{1}{2}\left(1+\frac{|\hat{U}_N|}{\hat{U}_e}\right)\cos\frac{\pi y}{\delta}, \tag{4.9}$$

then the momentum- and displacement-thickness integrals $\hat{\theta}$ and $\delta^*$ produce

$$\frac{|\hat{U}_N|}{\hat{U}_e} = \frac{4}{3}\left(1-\frac{1}{\hat{H}}\right)-1, \tag{4.10}$$

since $\hat{H} = \delta^*/\hat{\theta}$. The dashed line shown in figure 13 for this equation crosses the solid line.

The data are scattered, but they fall near these two lines. Even though $|\hat{U}_N|/\hat{U}_e$ is about $\pm 0.01$ uncertain, the hysteresis loop for a given streamwise location either

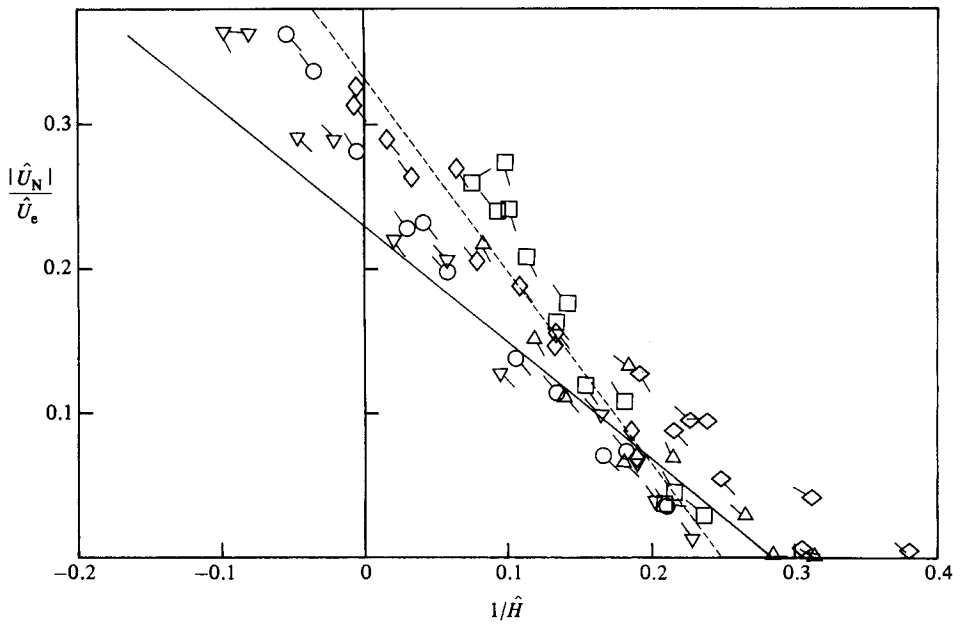


FIGURE 14. $|\hat{U}_N|/\hat{U}_e$ *vs.* $1/\hat{H}$ for the $k = 0.90$ flow. Solid line given by (4.8); dashed line given by (4.10). Leader on each symbol points in the local direction of a hysteresis loop for a given streamwise location: ◇, 3.00 m; △, 3.25 m; □, 3.45 m; ◇, 3.67 m; ○, 3.98 m; ▽, 4.34 m.

is parallel to or follows the steady-flow line when $|\hat{U}_N|/\hat{U}_e$ is increasing. There is a general tendency for the data to follow (4.10) when $|\hat{U}_N|/\hat{U}_e$ is decreasing.

Figure 14 shows $|\hat{U}_N|/\hat{U}_e$ *vs.* $1/\hat{H}$ for the present unsteady flow. These data have larger hysteresis loops than in figure 13, with also a general tendency for the data to follow or be parallel to the steady-flow line when $|\hat{U}_N|/\hat{U}_e$ is increasing. A significant difference with figure 13 is that $|\hat{U}_N|/\hat{U}_e$ reaches large values with negative values of $1/\hat{H}$. Figure 10 shows ensemble-averaged velocity profiles for $\hat{\gamma}_{pu\,\min} \approx 0.01$ for such conditions. $\hat{H}$ is a large-magnitude negative quantity during minimum $\hat{\gamma}_{pu\,\min}$ conditions because $\hat{\theta}$ is very small and negative.

In still another parameter cross-plot, figure 15 shows $|\hat{U}_N|/\hat{U}_e$ *vs.* $\hat{\gamma}_{pu\,\min}$ for the steady flow and the high-speed unsteady flow. No data fall below the solid line given by

$$\frac{|\hat{U}_N|}{\hat{U}_e} = -0.0677 \ln|\hat{\gamma}_{pu\,\min}| - 0.047, \tag{4.11}$$

while

$$\frac{|\hat{U}_N|}{\hat{U}_e} = -0.0754 \ln|\hat{\gamma}_{pu\,\min}| - 0.052 \tag{4.12}$$

describes a mean-square fit through the steady-flow data. The hysteresis loops are clockwise and are progressively greater in the downstream direction. When $\hat{\gamma}_{pu\,\min}$ decreases, $|\hat{U}_N|/\hat{U}_e$ increases in approximately the same way as for the steady free-stream detached flow. The peak value of $|\hat{U}_N|/\hat{U}_e$ at each station occurs at 330°, or lags the free-stream velocity oscillation by about 110°–130°.

Figure 16 shows the $k = 0.90$ results. Some of the data for $\partial\hat{\gamma}_{pu\,\min}/\partial t < 0$ fall below (4.11), but only when $\hat{\gamma}_{pu\,\min}$ is near zero where the uncertainty for $\hat{\gamma}_{pu\,\min}$ is comparable to $\gamma_{pu\,\min}$. Clockwise hysteresis loops are larger than for the $k = 0.61$ flow. The peak value of $|\hat{U}_N|/\hat{U}_e$ at each station occurs at 20°, thus lagging the free-stream

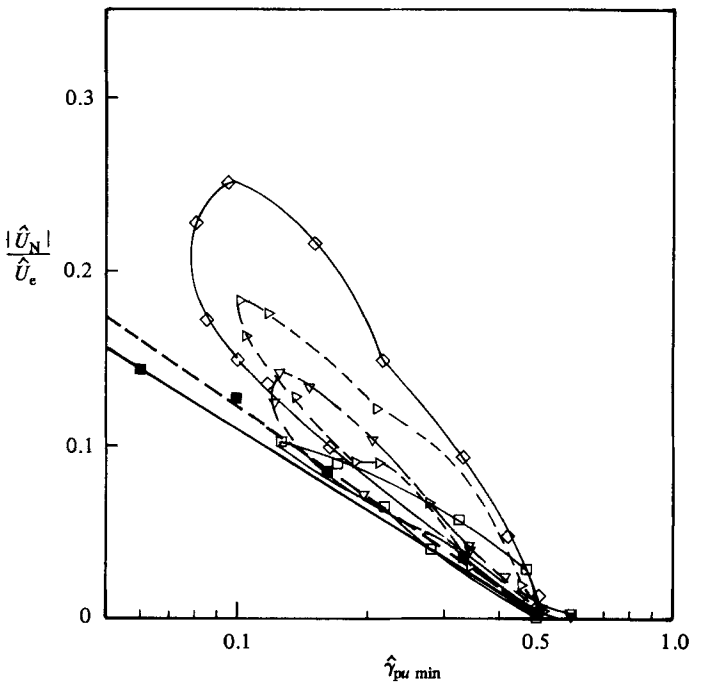


FIGURE 15. $|\hat{U}_N|\ \hat{U}_e$ *vs.* $\hat{\gamma}_{pu\,min}$: ■, steady flow of Simpson *et al.* (1981*a*); unsteady flow, $k = 0.61$, with clockwise hysteresis loops: ——□, 3.52 m; – – –▽, 3.68 m; - - - -▽, 3.97 m; ——◇, 4.34 m. Solid straight line given by (4.11); dashed straight line given by (4.12).

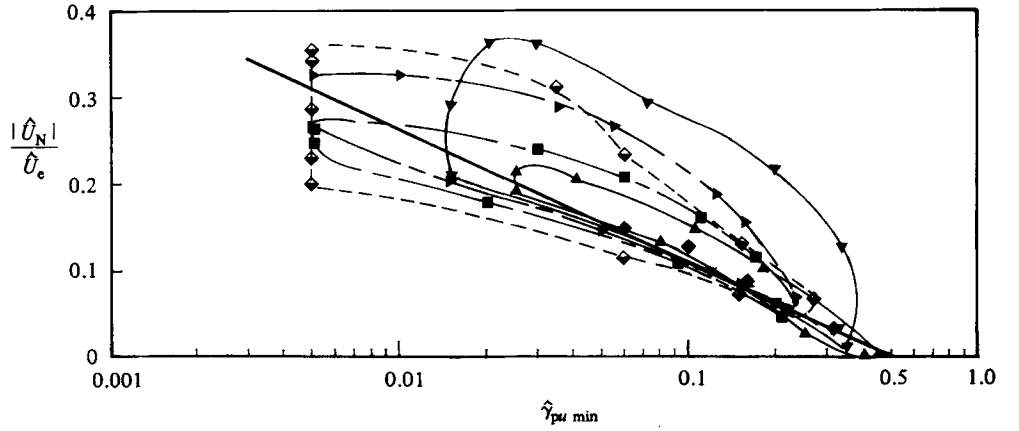


FIGURE 16. $|\hat{U}_N|/\hat{U}_e$ *vs.* $\hat{\gamma}_{pu\,min}$: ◆, steady flow of Simpson *et al.* (1981*a*); unsteady flow, $k = 0.90$, with clockwise hysteresis loops: ——▲, 3.25 m; – – –■, 3.45 m; – – –▲, 3.67 m; - - - -◆, 3.98 m; ——▼, 4.34 m. Solid straight line given by (4.11).

velocity oscillation by about 120°–150°. In both plots, $|\hat{U}_N|/\hat{U}_e$ increases substantially during the minimum $\hat{\gamma}_{pu\,min}$ phases. The dip in $\hat{\gamma}_{pu\,min}$ shown in figure 8 between the double peaks is obscured in figure 16 by the density of data for $0.1 < \hat{\gamma}_{pu\,min} < 0.5$.

Figure 17 shows the distance $\hat{M}$ from the wall to where $\hat{\gamma}_{pu}$ is 0.99 *vs.* $\hat{\gamma}_{pu\,min}$ for the two steady flows of Simpson *et al.* (1977, 1981*a*) and the $k = 0.90$ unsteady flow. The relatively large uncertainty bands for the steady-flow data are shown in this

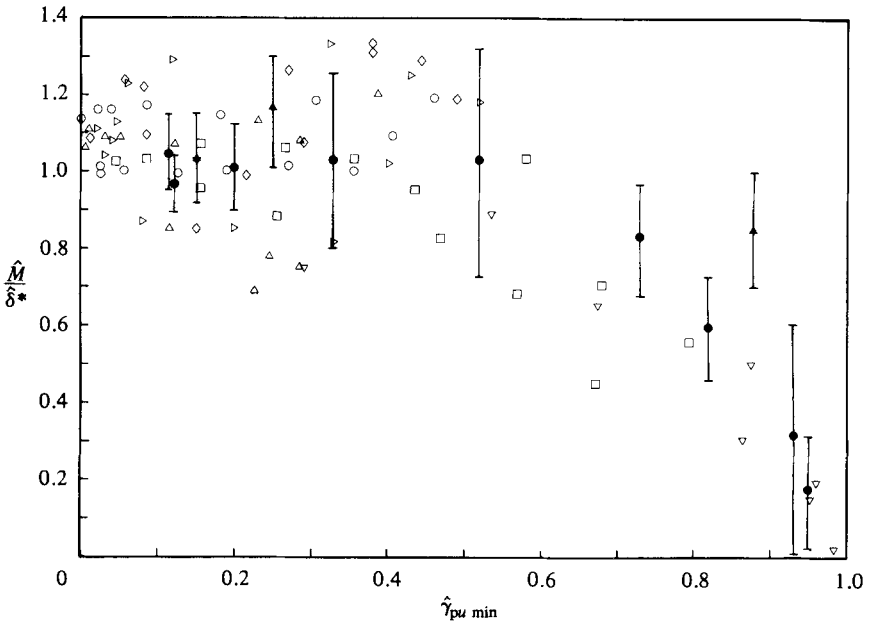


FIGURE 17. Distance $\hat{M}$ from wall to where $\hat{\gamma}_{pu}$ is 0.99, normalized on $\delta^*$. Steady-flow data: ▲, Simpson *et al.* (1977); ●, Simpson *et al.* (1981). Note the uncertainty bands. Unsteady flow, $k = 0.90$: ▽, 3.00 m; □, 3.25 m; △, 3.45 m; ◇, 3.67 m; ○, 3.98 m; ▽, 4.34 m.

figure and are due mainly to the uncertainty in $M$. Similar uncertainty values apply to the unsteady-flow data. For $\hat{\gamma}_{pu\,\min} < 0.5$, $M/\delta^*$ is nearly constant at unity for the steady-flows, and decreases to zero as $\hat{\gamma}_{pu\,\min}$ approaches unity. The lower-value unsteady-flow data occur during phases of the cycle when the free-stream velocity is near maximum. High data points occur during minimum free-stream velocity phases of the cycle.

## 5. Conclusions

Experimental data for a $k = 0.90$ unsteady free-stream separating turbulent boundary layer have been presented and compared with the $k = 0.61$ data of Simpson *et al.* (1983). Both flows had nearly sinusoidally varying free-stream velocity waveforms with a velocity amplitude to mean value of about $\frac{1}{3}$. Both flows had nearly the same streamwise oscillating and mean-pressure-gradient distributions, with the exception of the detached-flow zone, where the amplitude of the pressure gradient oscillation for the $k = 0.90$ flow was about $\frac{2}{3}$ that for the $k = 0.61$ flow. Downstream of detachment, the free-stream velocity and pressure gradient are in phase. At 3.98 m in the $k = 0.61$ flow, $\omega\delta^*/2\overline{U}_e = 0.020$, while $\omega\delta^*/2\overline{U}_e = 0.043$ for the $k = 0.90$ case.

Upstream of where $\hat{\gamma}_{pu} < 1$, both flows have a quasisteady structure. A semilogarithmic velocity-profile region exists with a constant phase angle. The phase-angle variation from the wall through the boundary layer is small. The ratio of oscillation and mean wall-shearing stresses is twice the ratio of the oscillation and mean velocities in the semilogarithmic region. Just upstream of where $\hat{\gamma}_{pu} < 1$, the Perry & Schofield (1973) velocity-profile correlations fit ensemble-averaged velocity profiles.

Downstream of detachment, the near-wall mean backflow velocity profiles for both

unsteady flows agree with the steady free-stream result and scale on the maximum negative mean velocity $|\overline{U}_N|$ and its distance $\overline{N}$ from the wall. Since the phase angle of the periodic flow and $\tilde{U}_1/|\overline{U}|$ for this near-wall region are nearly constant, this same normalized profile applies to phase-averaged profiles when scaled on $|\hat{U}_N|$ and $\hat{N}$. In both flows the near-wall phase angle in the backflow has a progressively greater phase lead over the free-stream pressure gradient as one proceeds downstream, approaching 135° asymptotically.

In both unsteady flows, the ensemble-averaged detached-flow velocity profiles $\hat{U}/\hat{U}_e$ *vs.* $y/\hat{\delta}^*$ agree with steady free-stream profiles for the same value of $\hat{\gamma}_{pu\,min}$ when $\partial\hat{\gamma}_{pu\,min}/\partial t < 0$. However, the $k = 0.90$ flow has much larger hysteresis in ensemble-averaged velocity-profile shapes when $\partial\hat{\gamma}_{pu\,min}/\partial t \geqslant 0$. Larger and negative values of $\hat{H}$ occur for this flow during phases when $|\hat{U}_N|/\hat{U}_e$ is large and $\hat{\gamma}_{pu\,min} \to 0.01$ because of small and negative $\hat{\theta}$-values. Peak values of $|\hat{U}_N|/\hat{U}_e$ lag the peak free-stream velocity by about 110°–130° in the $k = 0.61$ flow and by about 120°–150° in the $k = 0.90$ flow.

For both unsteady flows, the location where $\hat{\gamma}_{pu\,min}$ is less than unity moves downstream and $\hat{\gamma}_{pu\,min}$ increases at all downstream locations as backflow is washed downstream. Since the adverse pressure gradient is almost in phase with the free-stream velocity, it also increases and causes progressively greater backflow at downstream locations as the free-stream flow increases, while $\hat{\gamma}_{pu\,min}$ remains high upstream. During this part of the cycle for the $k = 0.90$ flow, $\hat{\gamma}_{pu\,min}$ *vs.* $\omega t$ plots show double peaks on each side of a local minimum at 135° between the 3.25 m and 3.53 m locations. At later phases $\hat{\gamma}_{pu\,min}$ has lower values at downstream locations than in the $k = 0.61$ flow. As the free-stream velocity decreases, the location where $\hat{\gamma}_{pu\,min}$ is less than unity moves upstream, as in the $k = 0.61$ flow.

Thus, while both unsteady flows have the same qualitative behaviour, the higher reduced frequency shows more hysteresis effects in the ensemble-averaged velocity profiles.

This work was supported by the U.S. Army Research Office under Grant DAAG29-72-G-0187 and the National Aeronautics and Space Administration, Ames Research Center, Experimental Fluid Dynamics Branch, under Grant NSG-2354, monitored by J. G. Marvin. The authors would like to thank Messrs G. Kokolis, J. Sallas, and Dr R. E. Nasburg for their aid in this research.

## REFERENCES

COUSTEIX, J., HOUDEVILLE, R. & JAVELLE, J. 1981 *Unsteady Turbulent Shear Flow*, pp. 120–139. Springer.

DAVIS, R. E. 1974 *J. Fluid Mech.* **63**, 673–693.

HASTINGS, R. C. & MORETON, K. G. 1982 *Intl Symp. on Applications of Laser Doppler Anemometry to Fluid Mech., Lisbon, 5–7 July, paper* 11.1.

HOUDEVILLE, R. & COUSTEIX, J. 1979 *La Recherche Aérospatiale*, 1979–1, *NASA* Tr TM75799-N 8017400.

PERRY, A. E. & SCHOFIELD, W. H. 1973 *Phys. Fluids* **16**, 2068–2074.

PHILLIPS, O. M. 1955 *Proc. Camb. Phil. Soc.* **51**, 220–229.

SHILOH, K., SHIVAPRASAD, B. G. & SIMPSON, R. L. 1981 *J. Fluid Mech.* **113**, 75–90.

SHIVAPRASAD, B. G. & SIMPSON, R. L. 1982 *Trans. ASME* I: *J. Fluids Engng* **104**, 162–166.

SIMPSON, R. L. 1977 *Paper* 19, *AGARD*-CP-227.

SIMPSON, R. L. 1983 *AIAA J.* **21**, 142–143.

SIMPSON, R. L., CHEW, Y-T. & SHIVAPRASAD, B. G. 1980*a* *Project SQUID Rep.* SMU-4-Pu; *NTIS* AD-A095 252/3.

SIMPSON, R. L., CHEW, Y-T. & SHIVAPRASAD, B. G. 1980*b* *Dept Civil/Mech. Engng Rep.* WT-6, *Southern Methodist University*; *NTIS* Ad-A090 585/1.

SIMPSON, R. L., CHEW, Y-T. & SHIVAPRASAD, B. G. 1981 *a* *J. Fluid Mech.* **113**, 23–51.

SIMPSON, R. L., CHEW, Y-T. & SHIVAPRASAD, B. B. 1981 *b* *J. Fluid Mech.* **113**, 53–73.

SIMPSON, R. L., SHIVAPRASAD, B. G. & CHEW, Y-T. 1983 *J. Fluid Mech.* **127**, 219–261.

SIMPSON, R. L., STRICKLAND, J. H. & BARR, P. W. 1977 *J. Fluid Mech.* **79**, 553–594.

WESTPHAL, R. V. 1982 Ph.D. dissertation, Dept of Mechanical Engineering, Thermosciences Division, Stanford University.